Crustal structure beneath western and eastern Iceland from surface waves and receiver functions

Zhijun Du,[1] G. R. Foulger,[2] B. R. Julian,[3] R. M. Allen,[4] G. Nolet,[4] W. J. Morgan,[4] B. H. Bergsson,[5] P. Erlendsson,[5] S. Jakobsdottir,[5] S. Ragnarsson,[5] R. Stefansson[5] and K. Vogfjord[6]

[1]*Institute of Theoretical Geophysics, University of Cambridge, Downing Street, Cambridge* CB2 3EQ, *UK*

[2]*Department of Geological Sciences, University of Durham, South Road, Durham* DH1 3LE, *UK. E-mail: G.R.Foulger@durham.ac.uk; foulger@gps.caltech.edu*

[3]*US Geological Survey,* 345 *Middlefield Road, Menlo Park,* CA 94025, *USA*

[4]*Department of Geological and Geophysical Sciences, Guyot Hall, Princeton University, Princeton,* NJ 08544-5807, *USA*

[5]*Meteorological Office of Iceland, Bustadavegi* 9, *Reykjavik, Iceland*

[6]*National Energy Authority, Grensasvegi* 9, *Reykjavik, Iceland*

SUMMARY

We determine the crustal structures beneath 14 broad-band seismic stations, deployed in western, eastern, central and southern Iceland, using surface wave dispersion curves and receiver functions. We implement a method to invert receiver functions using constraints obtained from genetic algorithm inversion of surface waves. Our final models satisfy both data sets. The thickness of the upper crust, as defined by the velocity horizon $V_s = 3.7$ km s^{-1}, is fairly uniform at $\sim$6.5–9 km beneath the Tertiary intraplate areas of western and eastern Iceland, and unusually thick at 11 km beneath station HOT22 in the far south of Iceland. The depth to the base of the lower crust, as defined by the velocity horizon $V_s = 4.1$ km s^{-1} is $\sim$20–26 km in western Iceland and $\sim$27–33 km in eastern Iceland. These results agree with those of explosion profiles that detect a thinner crust beneath western Iceland than beneath eastern Iceland. An earlier report of a substantial low-velocity zone beneath the Middle Volcanic Zone in the lower crust is confirmed by a similar observation beneath an additional station there. As was found in previous receiver function studies, the most reliable feature of the results is the clear division into an upper sequence that is a few kilometres thick where velocity gradients are high, and a lower, thicker sequence where velocity gradients are low. The transition to typical mantle velocities is variable, and may range from being very gradational to being relatively sharp and clear. A clear Moho, by any definition, is rarely seen, and there is thus uncertainty in estimates of the thickness of the crust in many areas. Although a great deal of seismic data are now available constraining the structures of the crust and upper mantle beneath Iceland, their geological nature is not well understood.

Key words: crustal structure, crustal thickness, Iceland, receiver functions, surface waves.

INTRODUCTION

Iceland is an extensive subaerial exposure of the mid-Atlantic spreading plate boundary and adjacent flanking plates. In the south the plate boundary comprises two spreading zones: the Western and Eastern Volcanic Zones (WVZ, EVZ) (Fig. 1). In the north, spreading is taken along a single zone, the Northern Volcanic Zone (NVZ). In central Iceland the WVZ, EVZ and NVZ are connected by the Middle Volcanic Zone (MVZ).

The surface morphology of the plate west of the currently active spreading zones has been complicated by a series of progressive eastwards rift jumps that have left in their wake three old rift zones.

Extinct rift zones lie along the northwestern edge of the Western Fjords, and along the Skagi peninsula. The third old rift zone lies along the Snaefellsnes peninsula. This zone has not taken up spreading recently, but is still volcanically active, and for this reason it is classified as a flank zone (Saemundsson 1979). It is dominated by the 1450 m high active Snaefellsjokull volcano, which lies at its western extremity. The area east of the spreading zones is simpler, and not complicated by extinct rift zones. However, the Tertiary, intraplate areas of both eastern and western Iceland are densely intruded almost everywhere by extinct dyke and fault swarms, central volcanoes and calderas (Johannesson & Saemundsson 1998), and these areas are thus heterogeneous.
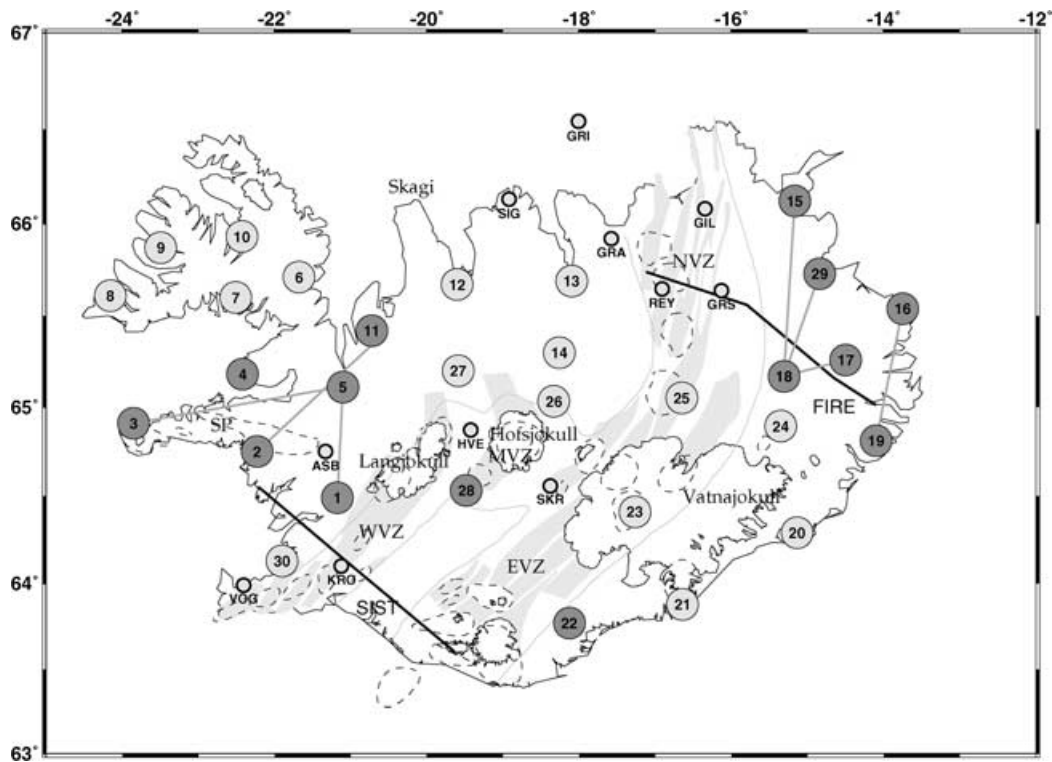
Figure 1. Map of Iceland outlining the neovolcanic zone and showing fissure swarms (grey), central volcanoes (dashed), glaciers (outlined) and the locations of stations of the Iceland Hotspot Project (large dots). Stations of the permanent Icelandic SIL network that had broad-band sensors are shown as small dots. Stations shown in dark grey were used in this study. The thick lines represent the SIST and FIRE explosion profiles (Bjarnason *et al.* 1993; Staples *et al.* 1997). Thin grey lines show the station-pair ray paths used to measure differential Rayleigh-wave phase velocities. WVZ = Western Volcanic Zone, MVZ = Middle Volcanic Zone, NVZ = Northern Volcanic Zone, EVZ = Eastern Volcanic Zone, SP = Snaefellsnes peninsula.

The structure of the Icelandic crust and upper mantle has been studied extensively using long explosion seismology profiles, and the results are all in broad agreement (e.g. Flovenz 1980; Angenheister *et al.* 1980; Flovenz & Gunnarsson 1991; Bjarnason *et al.* 1993; Staples *et al.* 1997; Darbyshire *et al.* 1998; Menke *et al.* 1998). The upper ∼5–10 km are characterized by steep gradients of up to ∼0.8 s^{-1} in V_p, below which lies a ∼15–30 km thick section of material with much lower velocity gradients of ∼0–0.02 s^{-1}. Reflective horizons at depths of ∼20–40 km have been observed in a few places, and have been interpreted as a Moho beneath Iceland, but refracted head waves are almost entirely unobserved from such horizons.

Explosion seismology profiles have only explored a few laterally restricted zones in Iceland, and furthermore, only small areas beneath the centres of the profiles are probed deeply. In order to extrapolate the results to unsampled areas, or areas sampled poorly by explosion seismology, the results have been combined with Iceland-wide gravity data (Darbyshire *et al.* 2000). This is an expedient approach where independent seismic structures are not available for all areas. However, a more powerful approach is to acquire independent seismic data everywhere. A combination of such results with gravity data may then be used to constrain other geological parameters.

Du & Foulger (1999, 2001) obtained crustal structures beneath 17 broad-band seismometer stations deployed in northwest and central Iceland during 1996–1998 by the Iceland Hotspot Project. They combined surface waves, receiver functions and waveform modelling to obtain structures with both well-constrained absolute velocities and small-scale details. Considerable variation in structural style was observed. Two end-member types were identified, and termed structures of the first and second types (Du & Foulger 1999).

Structures of the first type are characterized by a clear tripartite division into an upper section with high velocity gradients and a lower section with low velocity gradients, underlain by a clear velocity discontinuity or transition zone a few kilometres thick with high velocity gradients. Structures of the second type lacked this clear tripartite division, and to first order the velocity gradient decreased smoothly with depth. Most structures fell between these two extremes and showed some characteristics of both. In addition to this variation in basic structural style, considerable 3-D heterogeneity was demonstrated by the variation in results observed at individual stations for earthquakes arriving from different directions.

In this paper we present the results for an additional 14 stations of the Iceland Hotspot Project broad-band network in western, eastern, central and southern Iceland, thus completing a homogeneous set of structural results extending over most of Iceland. We follow the convention used earlier by Du & Foulger (1999, 2001), and assume the base of the upper crust to be the shallowest level at which V_s reaches 3.7 km s^{-1}, and the base of the lower crust to be the level below which V_s does not fall below 4.1 km s^{-1}. These values correspond to values of V_p of 6.5 and 7.2 km s^{-1}, assuming a V_p/V_s ratio of 1.76 (Menke *et al.* 1996), which are the average velocities found for the bases of the upper and lower crusts from explosion seismology profiles throughout Iceland.

Since the Icelandic crust is 3-D, a simple joint inversion of surface wave dispersion data and receiver functions is not, in general, successful. Du & Foulger (1999) addressed the problem of backazimuthal structural variation in the Western Fjords area with a joint inversion scheme using surface waves approaching from the same direction as the earthquakes used for receiver functions. In the case of central Iceland, Du & Foulger (2001) found significant structural

differences between the seismic station localities and their immediate neighbourhood. To deal with this problem they developed a joint estimation scheme involving combining modelling of surface wave dispersion curves, local earthquake waveforms, and receiver functions, and selected as their final results the mean models that satisfied all three data sets.

In this paper we study the structure beneath western and eastern Iceland, and two additional stations in central and southern Iceland. We develop a method to invert receiver functions using constraints obtained from independent inversion of surface wave dispersion curves using a genetic algorithm (GA). The new method keeps the long-wavelength features of the velocity model, i.e. the average velocities resolved by the surface waves, while using receiver functions to constrain the short-wavelength details. We also include in the new inversion scheme a data covariance matrix containing the measurement error of the receiver functions to prevent the inversion over- or underfitting the data, which may result in the inclusion of insignificant structural details in the final models.

We find that the depths to the bases of the upper and lower crusts for western Iceland are $\sim$6.5–7 and $\sim$20–26 km, and for eastern Iceland $\sim$7–9 and $\sim$27–33 km. These results are in broad agreement with those of explosion profiles, which find the thickness of the crust to be greater in eastern Iceland than in western Iceland (Bjarnason *et al.* 1993; Staples *et al.* 1997).

As is the case for northwest and central Iceland, the only clear, common feature of the results is the division into an upper section a few kilometres thick with high velocity gradients, and a thicker, lower section with low velocity gradients. The nature of the transition to typical mantle velocities at greater depth ranges from being relatively abrupt to being gradational. In these latter cases, there are thus inevitably large uncertainties in estimates of the depth to the base of the lower crust if the underlying mantle is assumed to have normal seismic velocities.

D A T A

Stations and earthquakes

We used data recorded on a network of broad-band seismic stations deployed in Iceland 1996–1998 by the Iceland Hotspot Project (Fig. 1). The network is described in detail by Du & Foulger (1999, 2001) and Foulger *et al.* (2001). The sensors deployed were three-component Guralp CMG-3ESP, 3 or 40 T seismometers, which have a flat velocity response in the frequency range 0.02 to 30–100 Hz. At the stations used in this study, data were recorded on Refraction Technology 72a-02 24 bit data loggers that recorded at 20 samples s^{-1}. Absolute timing was provided by the GPS.

We analysed seismograms from regional and teleseismic earthquakes recorded at 14 stations (Fig. 1). The 36 teleseismic events that we used for receiver functions were grouped into three backazimuths: north (backazimuths $\alpha = 357°$–$31°$, epicentral distances $\Delta = 60°$–$89°$), east ($\alpha = 70°$–$125°$, $\Delta = 36°$–$73°$) and southwest ($\alpha = 221°$–$280°$, $\Delta = 60°$–$89°$). Oceanic microseismic noise is strong in Iceland, and in order to suppress this we stacked receiver functions from similar backazimuths in limited epicentral ranges.

Receiver functions

We used the source-equalization method of frequency-domain receiver function analysis (Langston 1979), and followed a similar procedure to Du & Foulger (1999, 2001). We applied a Gaussian low-pass filter with a corner frequency of 1.2 Hz to remove high-frequency noise, and deconvolution was done using a spectral trough

filler, *c*, of 0.01–0.001. We formed receiver-function stacks for each station using three to seven high-quality waveforms with relatively high signal-to-noise ratios. The ± 1 standard deviation (σ) bounds of each stack were used to monitor its quality. The events chosen for inclusion were those that yielded narrow σ bounds. In some cases events were drawn from relatively wide azimuthal ranges (up to 55°) where they yielded small σ bounds, whereas more tightly clustered events were rejected if they increased the width of the σ bounds. This approach ensured that only very similar events were selected for stacking. Since receiver functions corresponding to events from different distances have large amplitude differences we scale the receiver functions to unit amplitude prior to stacking (Ammon 1991). Fig. 2 shows examples of data stacking from the three backazimuths at station HOT01. The $\pm 1\sigma$ bounds show how well particular phases of the waveform are determined. The degree to which stacking succeeded in suppressing noise is shown by the amplitudes of the stacked traces prior to the *P* arrival in the radial receiver functions (left-hand panels of Fig. 2), and the amplitudes of the stacked tangential receiver functions (right-hand panels of Fig. 2).

In Fig. 3, the stacked radial receiver functions for all 14 stations and all three backazimuths are shown. Clear waveform pattern changes may be seen from station to station and from backazimuth to backazimuth. Although the P_s arrival times are different for stations HOT17–HOT19, similarities may be seen in the waveforms, particularly in the first $\sim$8 s, for earthquakes from the same backazimuth. Stations HOT15, HOT16 and HOT29 also display similar features, but to a lesser extent. Stations in the western, central and southern regions show diverse waveforms, but the east and southwest backazimuthal waveforms of stations HOT01 and HOT02 are very similar to each other. No coherent multiples can been seen in any of the stacked waveforms.

Surface waves

We analysed the data using the FTAN (frequency–time domain analysis) package, of which a detailed description is given by Levshin *et al.* (1992) and papers referred to therein. The method has the ability to remove interfering, scattered body waves and higher-mode surface waves when extracting the fundamental-mode wave. We measured surface wave phase-velocity dispersion curves for interstation pairs as described by Du & Foulger (1999, 2001). As shown in Fig. 4 (dotted lines), surface waves from the teleseisms are in the period band 17–50 s (paths HOT01–HOT05, HOT03–HOT05, HOT18–HOT15 and HOT18–HOT17), and surface waves from the regional events are in the period band 6–37 s (paths HOT02–HOT05, HOT05–HOT11, HOT18–HOT29 and HOT16–HOT19). The accuracy of dispersion curve measurement could be affected by the short path-length between station pairs ($\sim$50–80 km), but timing errors are negligible in our digital data. Phase velocities were measured from filtered waveforms that showed simple dispersion, as described in detail in Du & Foulger (1999) (see Fig. 8 of that paper). We estimate the associated measurement errors to be $\sim$$\pm$0.1 km s^{-1} for regional events, which is about the same as found by Du & Foulger (1999) (see Fig. 9 of that paper). This is close to the scatter in the measured phase velocities between station pairs.

In the western region, we measured four interstation dispersion curves around station HOT05 (dotted lines, Fig. 4). In the eastern region, we measured three paths around station HOT18 and one between stations HOT16 and HOT19 (dotted lines, Fig. 4). The data differences among these dispersion curves show backazimuthal structural variation in the regions around stations HOT05 and HOT18. In the western region, the path HOT02–HOT05 has
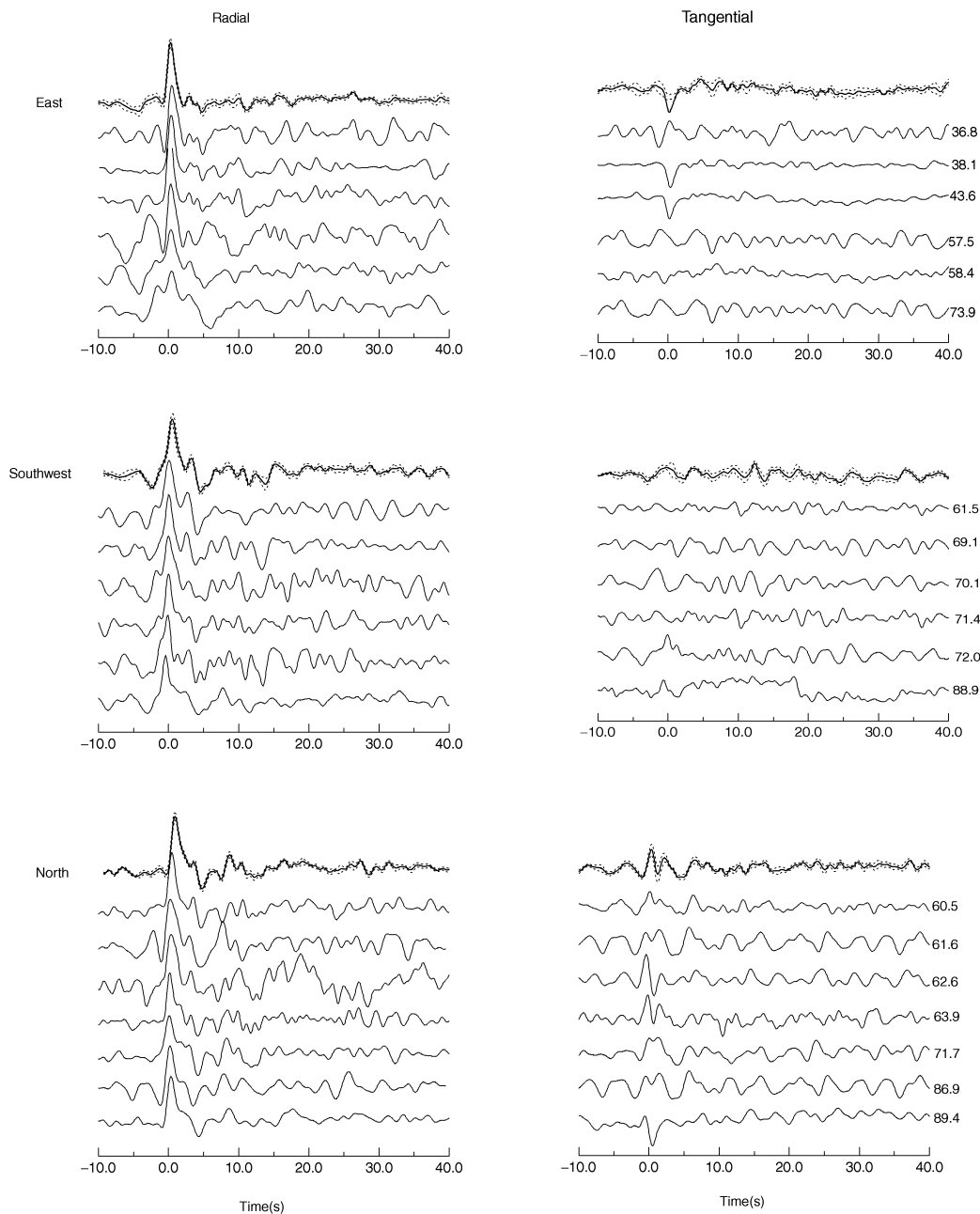
Figure 2. Examples of the stacking of receiver functions for station HOT01 from the east (top panels), southwest (middle panels) and north (bottom panels) backazimuths. Radial receiver functions are shown in the left-hand column and tangential receiver functions in the right-hand column. The top trace of each panel shows the stacked receiver function (thick line) and the one-standard-deviation bounds (dotted lines). Numbers on the right-hand side give the epicentral distances in degrees.

the lowest phase velocities. The path HOT16–HOT19 lies along the coast, and low phase velocities were found over the short-period band. These dispersion measurements do not coincide exactly with any of the three backazimuths used for the receiver functions. Nevertheless, the Rayleigh-wave phase-velocity dispersion curves reflect the broad average structures of these regions.

METHOD

The receiver-function method utilizes the waveforms of P_s conversions from velocity discontinuities to model variations in V_s beneath a seismic station (e.g. Ammon *et al.* 1990). The method is sensitive to velocity discontinuities, but it can only detect the velocity–depth product, and not absolute velocity. Independent constraints on absolute velocity from other sources are thus required. Surface waves are a convenient source of such information since both they and the receiver functions may be obtained from the same seismic station, dispensing with the need for an independent experiment. However, to obtain meaningful structures by combining receiver-function and surface wave data, the structural volume sampled by both data sets must be similar (Du & Foulger 1999), otherwise there is a risk of merging information from different structures. Where there is no large structural variation between a seismic station locality and its immediate neighbourhood, a good local structural model may
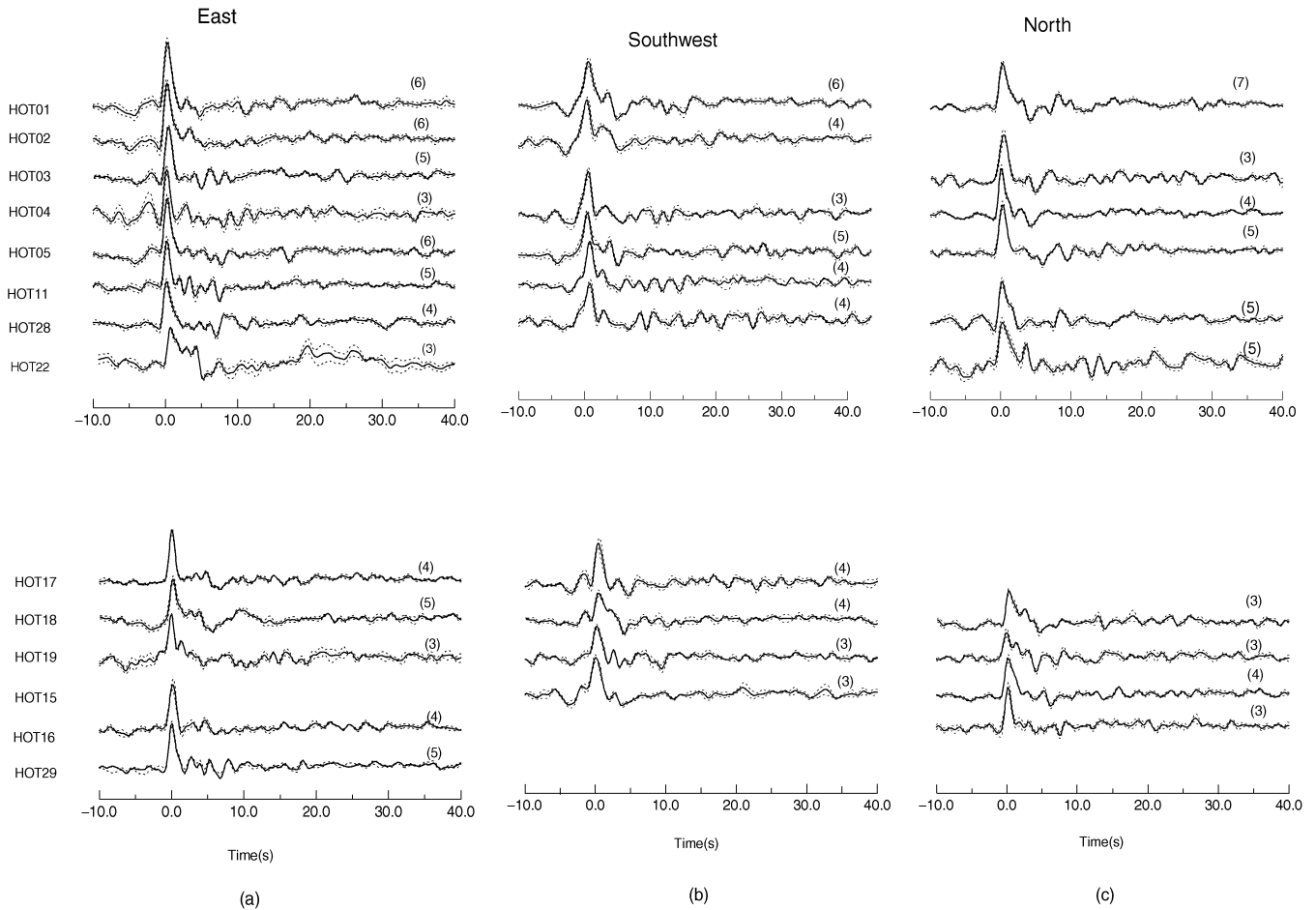
Figure 3. Top: stacked radial receiver functions for stations HOT01–HOT05, HOT11, HOT28 and HOT22 for the backazimuths (a) east, (b) southwest and (c) north. The one-standard-deviation bounds are shown as dotted lines. Numbers in parentheses give the number of seismograms stacked. Bottom: same as top, but for stations HOT15–HOT19 and HOT29.

be found by inversion of the dispersion velocities between station pairs.

Surface wave inversion using a genetic algorithm

We first use a genetic algorithm to invert the phase-velocity dispersion curves prior to inverting the receiver functions for 1-D shear-wave velocity structures. The GA is a non-linear, guided, global-search method, which efficiently searches a large model space, finding solutions that are nearly globally optimum. In this it is superior to many other techniques, e.g. damped least squares or conjugate gradient methods, which often find solutions that are only locally optimum (Sambridge & Drijkoningen 1992; Lomax & Snieder 1995). We briefly describe the basic methodology, illustrated through an example. A comprehensive review of the method is given by Goldberg (1989) and Davis (1990).

In our use of the GA, we define the depths of layer boundaries and the shear-wave velocities in the layers as our model parameters. We refer to the ith model parameter, of whichever type, as x_i, and constrain its value to lie between bounds a_i and b_i (Fig. 5a), so that $a_i \leq x_i \leq b_i$. By choosing appropriate bounds, it is easy to ensure that the layer boundaries remain in the correct order and layers do not overlap. We also require that x_i can take on only a finite number N_i of evenly spaced possible values, where N_i is a power of 2. The discretization interval for the ith parameter is thus

$$d_i = (b_i - a_i)/N_i \tag{1}$$

and each possible value for x_i may be encoded by an integer j:

$$x_i = a_i + j d_i \quad (j = 0, 1, 2, \dots, N_i). \tag{2}$$

We represent each such integer as a binary string, and concatenate the integers for all x_i to form a 'chromosome'. If n is the total number of bits in a chromosome, the number of possible models is 2^n.

The GA starts with a random initial population of chromosomes, i.e. a set of different binary strings. The rms data-misfit value is computed by solving the forward problem for the model corresponding to each chromosome in the population. The population then 're-produces' for a number of 'generations', with the poorly adapted individuals (those with rms residuals above the 95th percentile of the distribution for the first generation) being removed from the population at each generation. To create a new generation, we group the population randomly into pairs of 'parents' and pass their chromosomes to two 'offspring' for each pair, after possibly subjecting them to two kinds of changes in the process. First, 'crossing over' may occur, with a certain probability P_c that the chromosomes of the parents may be cut at a random position with one end of the resulting segments being exchanged. Second, 'mutations' may occur; each bit in the chromosomes may have its parity reversed with probability P_m. We assign both probabilities with an exponential decay
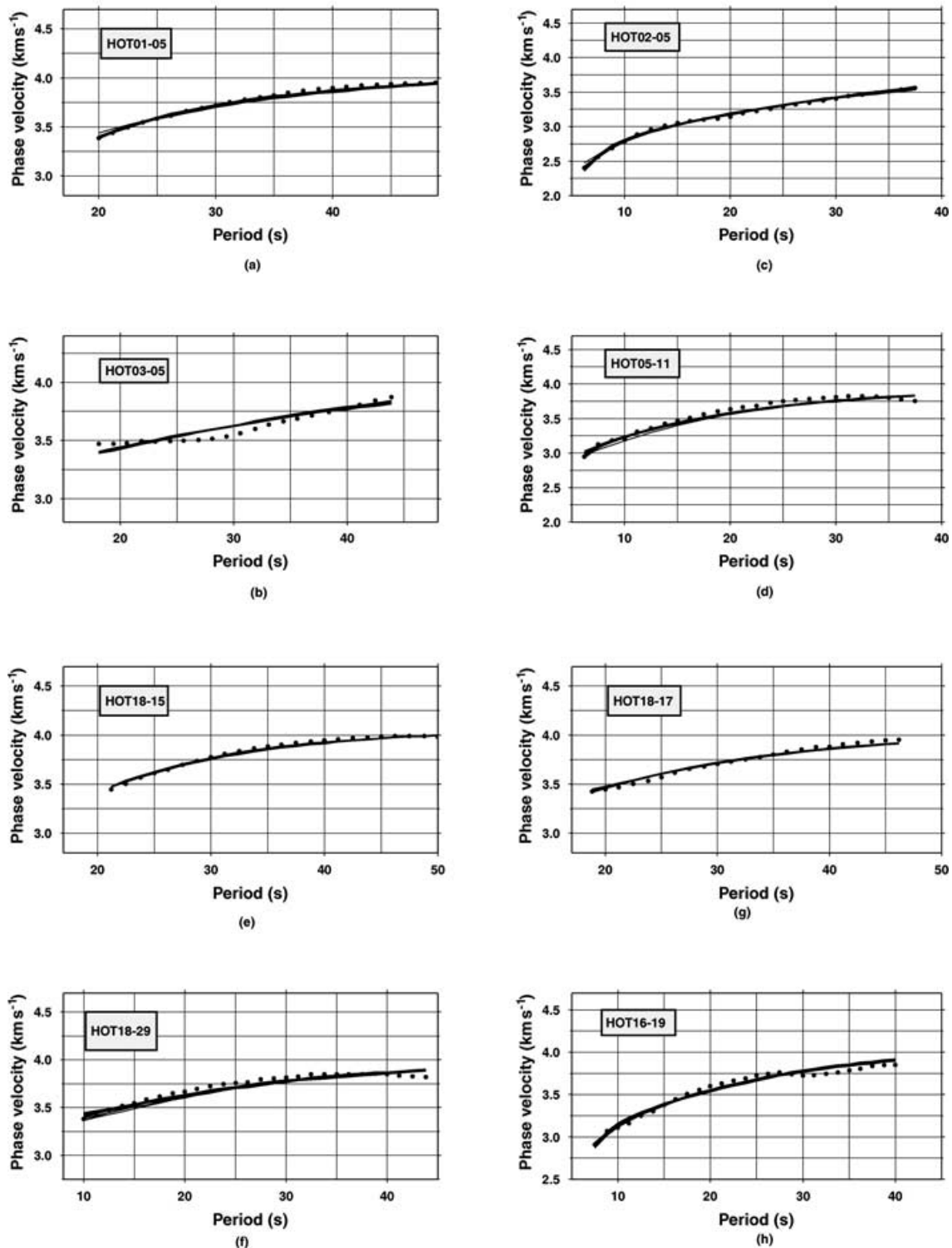
Rayleigh wave dispersion curves

Figure 4. Interstation Rayleigh-wave phase-velocity dispersion curves for: (a) path HOT01–HOT05, measured using event E97.339.11.54.96 ($M_s = 7.7$, $\alpha = 161.90°$, $\delta = 59.2°$) from the east coast of Kamchatka; (b) path HOT03–HOT05, measured using event E97.130.08.33.65 ($M_s = 7.3$, $\alpha = 59.73°$, $\delta = 53.4°$); (c) path HOT02–HOT05; (d) path HOT05–HOT11, measured using event E98.056.19.53.94 ($M_s = 5.5$, $\alpha = -35.22°$, $\delta = 14.0°$); (e) path HOT18–HOT15, measured using event E97.339.11.54.96 ($M_s = 7.7$, $\alpha = 161.90°$, $\delta = 59.2°$); (f) path HOT18–HOT29, measured using event E98.056.19.53.94 ($M_s = 5.5$, $\alpha = -35.22°$, $\delta = 14.0°$); (g) path HOT18–HOT17, measured using event E97.130.08.33.65 ($M_s = 7.3$, $\alpha = 59.73°$, $\delta = 53.4°$) and (h) path HOT16–HOT19, measured using event E98.080.16.79.89 ($M_s = 6.1$, $\alpha = 1.86°$, $\delta = 16.0°$). The heavy dots show the observations and bundles of lines show the curves predicted by the GA inversion results.
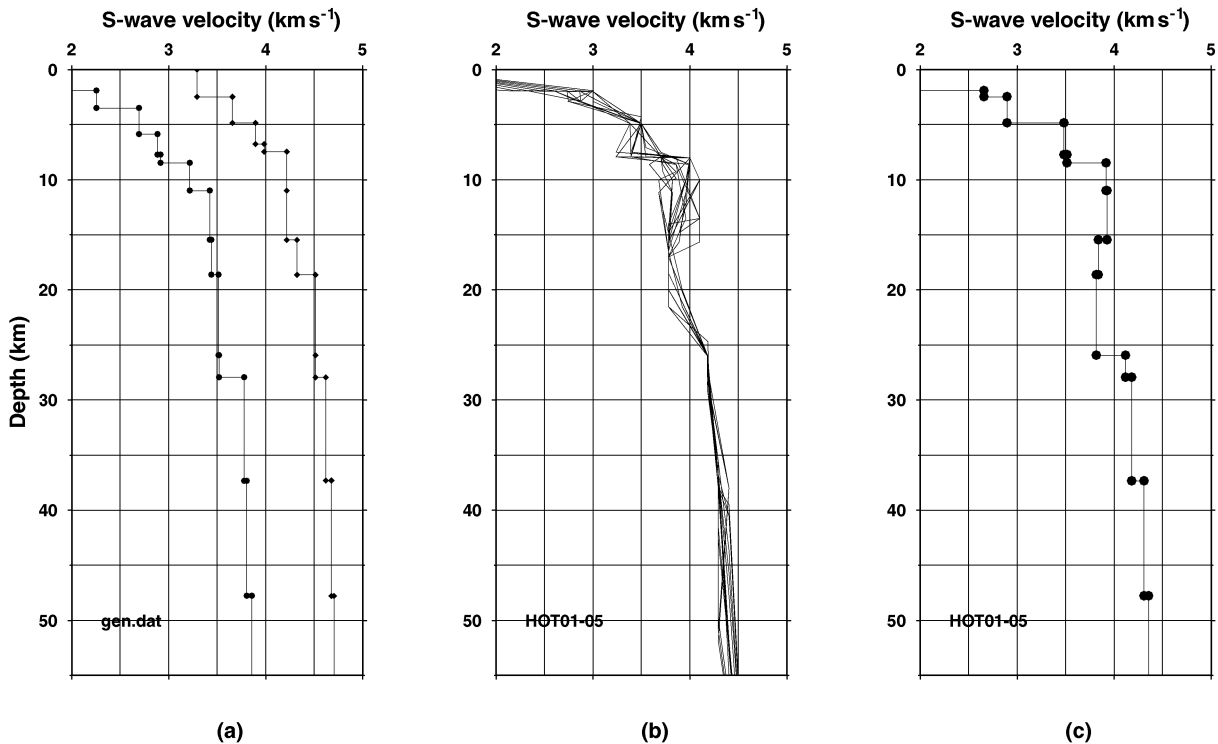
Figure 5. Inversion of a surface wave dispersion curve using the genetic algorithm. (a) Parameter bounds set on the model space, (b) results from the inversion of path HOT01–HOT05 (Fig. 4a) and (c) the average model from the family of GA results shown in (b).

algorithm (Sambridge & Drijkoningen 1992). This procedure is repeated for a prescribed number of generations.

The steps in the GA inversion are shown in Fig. 5. We parametrize the model using a layered structure. The free parameters of the inversion are the z coordinates and associated S-wave velocities. We use a V_p/V_s ratio of 1.76 (Menke *et al.* 1996) to obtain P-wave velocities from S-wave velocities. Within a GA, only very rough *a priori* structural information is required. We set the S-wave velocity model variation range as large as 0.5–1.0 km s^{-1}, and the depth range to be 1–4 km for shallow depth nodes and 5–12 km for deeper nodes (Fig. 5a). The exponential decay bounds for P_c are 0.8 and 0.6, and for P_m they are 0.02 and 0.001. We fit the observed dispersion curve allowing ±0.1 km s^{-1} error, which was estimated to be the rms error in the measurements made using the FTAN package (Levshin *et al.* 1992). We ran the inversion for 20 iterations. The family of best solutions obtained after each generation (using a maximum generation count of 30) is shown in Fig. 5(b) for path HOT01–HOT05. Fig. 5(c) is an average of Fig. 5(b).

Fig. 4 (solid lines) shows the fits of theoretical surface wave dispersion curves generated from the final GA models to the dispersion curves and Figs 6 and 7 give the final structural models. Surface wave phase velocities constrain discontinuities only weakly, and map them into broad, average S-wave velocities. Velocity gradients are high in the top ∼10 km and zero or small beneath this. In some profiles, e.g. HOT18–HOT15, velocity gradients increase again at greater depths and this may indicate deep velocity discontinuities. Inversions of the dispersion curves for some paths, e.g. HOT02–HOT05 and HOT05–HOT11, show little evidence for such velocity gradient increases. Paths HOT18–HOT15 and HOT17–HOT18 show deep zones of enhanced velocity gradient at depths of ∼30 and ∼25 km, respectively, while the results for paths HOT18–HOT29 and HOT16–HOT19 show smoother structures. The shallowest section in all the structures obtained has high velocity gradients, as

expected for the upper crust. The thickness of this section, although poorly constrained by surface waves alone, lies in the range ∼5–10 km.

Receiver function inversion

Following the general method of solving ill-posed inverse problems (e.g. Tarantola 1987) the problem of receiver-function inversion may be expressed as finding the minimum of a misfit function, **F**(**m**), for model parameters **m**,

$$\mathbf{F}(\mathbf{m}) = \|s(t) - S_{\text{syn}}(t, \mathbf{m})\| + \theta \|\mathbf{m} - \mathbf{m}_{\text{ref}}\| \tag{3}$$

where $s(t)$ and $S_{\text{syn}}(t, \mathbf{m})$ are, respectively, the receiver-function data and the synthetics computed from model **m**. $\mathbf{m}_{\text{ref}}$ is the selected reference model and θ is a Lagrange multiplier. The optimum parameters of the model can be found by an iterative minimization procedure, as described by Ammon *et al.* (1990), who used a smoothed least-squares scheme.

In practice, eq. (3) represents a local linearization of the misfit function, F, which requires that $\mathbf{m}_{\text{ref}}$ is close to the 'real' model. For receiver-function inversion the solutions for eq. (3) are ambiguous because of the trade-off between depth and velocity (Ammon *et al.* 1990). As a result, additional independent constraints are required to distinguish between different models that fit the data equally well.

We use $\mathbf{C}_d$ to describe our receiver-function data covariance to include the estimated standard squared error σ^2, i.e. $\mathbf{C}_d^{-1} = \text{diag}\{1/\sigma_1^2, \ldots, 1/\sigma_N^2\}$. N is the number of points of $s(t)$, and $\mathbf{C}_m$ comprises the model covariance between models **m** and $\mathbf{m}_{\text{ref}}$, which contains *a priori* model parameter information. We may then reformulate eq. (3) as

$$\mathbf{F}(\mathbf{m}) = \Delta \mathbf{d}^{\text{T}} \mathbf{C}_d^{-1} \Delta \mathbf{d} + \theta \Delta \mathbf{m}^{\text{T}} \mathbf{C}_m^{-1} \Delta \mathbf{m} \tag{4}$$

where $\Delta \mathbf{d}$ and $\Delta \mathbf{m}$ are the data and model residual vectors, respectively.
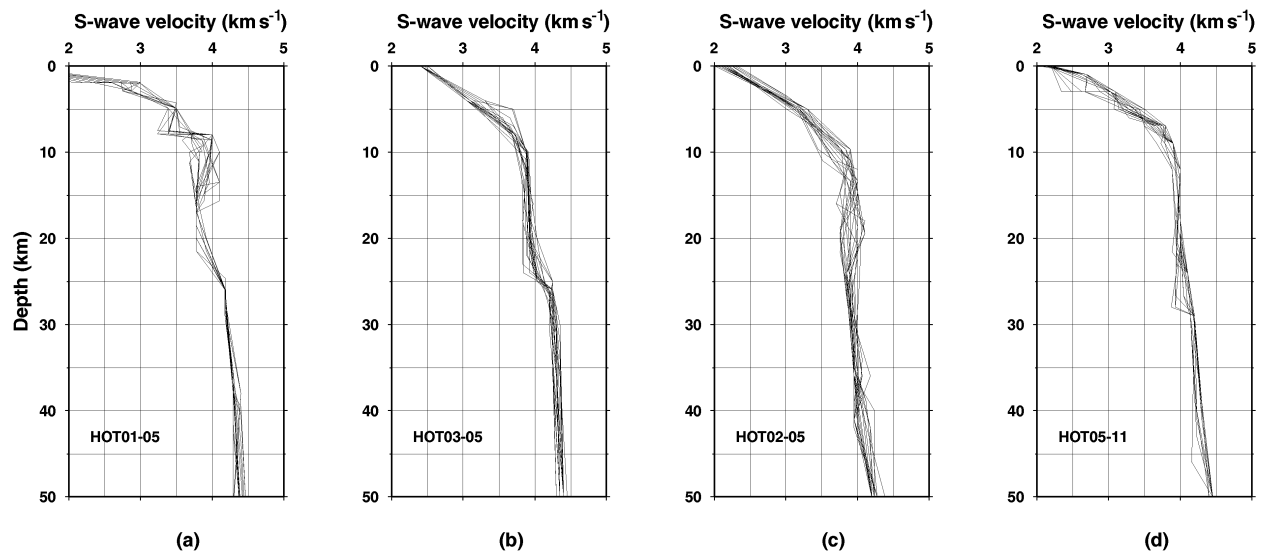
Figure 6. Velocity-depth profiles showing the families of structures obtained from GA inversion of the surface wave dispersion curves shown in Fig. 4. Results shown are: (a) for path HOT01–HOT05; (b) for path HOT03–HOT05, (c) for path HOT02–HOT05 and (d) for path HOT05–HOT11.

In eq. (4), $\mathbf{C}_m$ can be chosen and constructed to allow $\mathbf{m}$ to pick up the 'shape' of $\mathbf{m}_{ref}$, by adjusting θ, which also defines the damping. When the model term is updated after each iteration, the updated model, $\mathbf{m}$, tends to select the member of the solution set that is closest to $\mathbf{m}_{ref}$.

With the use of accurate *a priori* model-space information, it is possible to exploit the behaviour of $\mathbf{F}(\mathbf{m})$ locally. In each GA inversion an average model is determined (e.g. Fig. 5c). This model is used here as $\mathbf{m}_{ref}$. We select $\mathbf{C}_m$ to be diagonal, and parametrize it such that the model covariance is $\sim$0.1–0.3 (the estimated average error bounds of the GA inversion) to estimate the discrepancies between $\mathbf{m}$ and $\mathbf{m}_{ref}$.

We tested the sensitivity of the receiver function fits by limiting a few $\mathbf{C}_m$ values to 0.1–0.2 at those depths where $\mathbf{m}_{ref}$ shows smooth

velocity gradients, in favour of the GA inversion. We found that the incorporation of three to five such control points within $\mathbf{C}_m$, constraining the structure at features common in the different GA models, provides the information needed to minimize the velocity–depth ambiguity of the receiver function inversion. In this way, we keep the long-wavelength structural features resolved by the surface wave data and allow short-wavelength structural details to be resolved by the iterative receiver-function inversion. We then conduct a suite of inversions with a varying, smooth weighting using the approach of Ammon *et al.* (1990). An example of the results of inversions for the three backazimuthal data sets for station HOT01 is shown in Fig. 8. The receiver-function inversions improved upon the reference model obtained from the GA surface wave dispersion inversion by adding fine structure to it. The lower rightmost panel
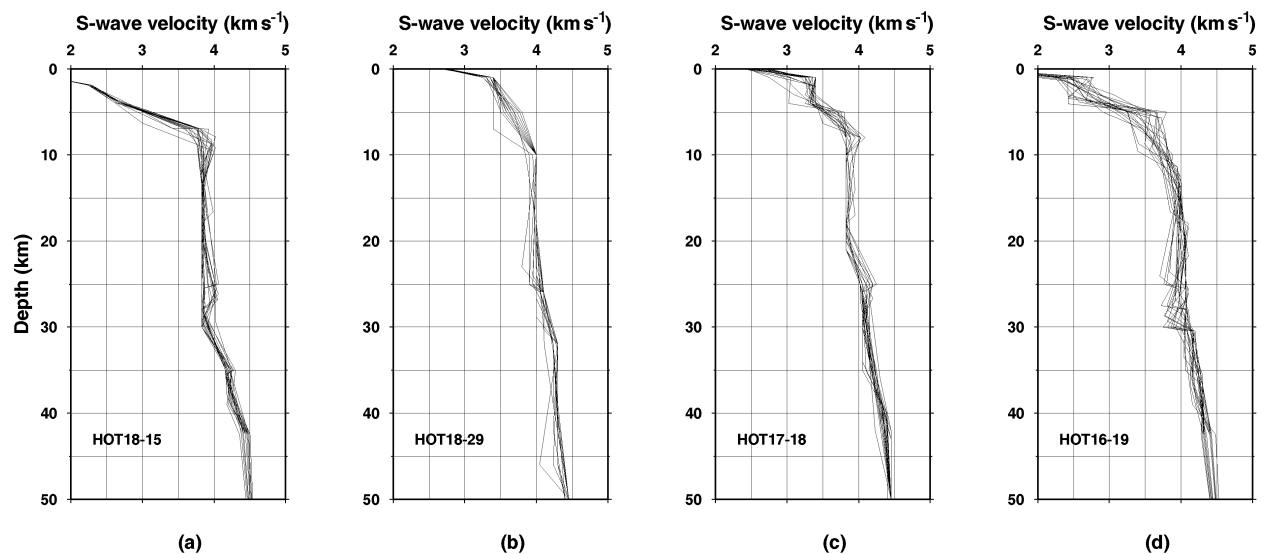

Figure 7. Same as in Fig. 6, but for paths in eastern Iceland. (a) HOT18–HOT15; (b) HOT18–HOT29; (c) HOT17–HOT18 and (d) HOT16–HOT19. The model predictions of surface wave dispersion curves are shown in Fig. 4 as bundles of lines.
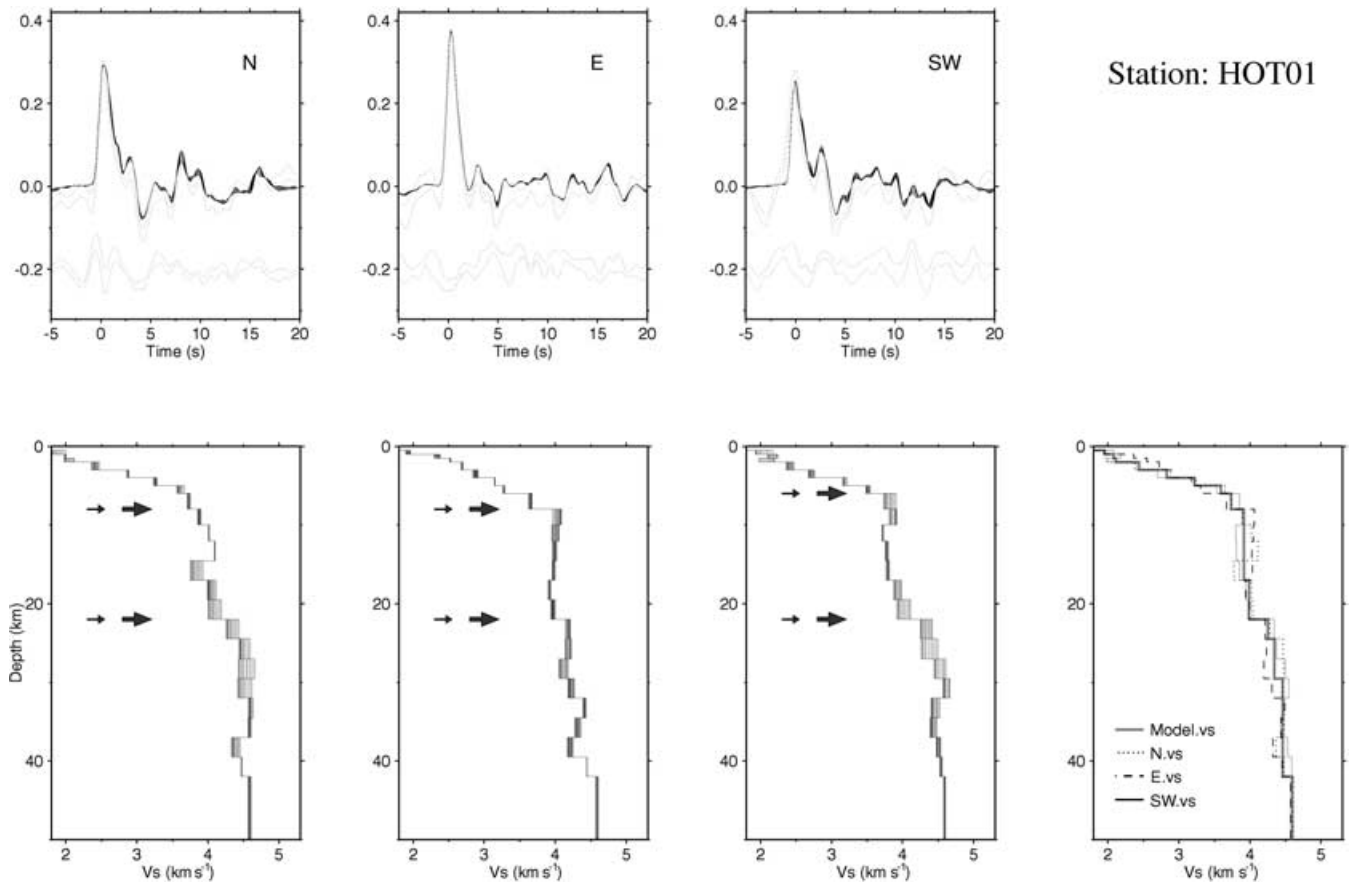
Figure 8. Receiver function inversion results for station HOT01. Upper panels show measured $\pm 1\sigma$ bounds of the radial (top) and tangential (bottom) receiver function data (dotted lines) and synthetic radial receiver functions computed from each inversion solution model (bundle of solid lines). The peak amplitude at time zero corresponds to an average value of event ray parameters used in forming the stack. Lower panels show the inversion solution models. The rightmost lower panel shows a summary of the inversion in the form of the smoothest model from each backazimuth (thin solid, dotted and dashed lines) and an overall average model (thick grey line). Small arrows show the depths at which V_s reaches 3.7 km s^{-1} and the depth beneath which it does not fall below 4.1 km s^{-1}. Large arrows show the best estimates of the depths to the bases of the upper and the lower crust.

of Fig. 8 summarizes the inversion results, showing the smoothest models from each backazimuthal inversion and an overall average model.

RESULTS

Crustal structures beneath western, central and southern Iceland

Stations HOT01–HOT05 and HOT11 lie in the Tertiary intraplate area west of the currently active WVZ and its northern extension, the extinct Skagi zone (Fig. 1). Station HOT03 lies at the foot of the Snaefellsjokull volcano, at the westerly extremity of the Snaefellsnes flank zone, and station HOT02 lies close to the southeastern border of this zone. Stations HOT04 and HOT11 lie within, or close to, extinct volcanic systems. Station HOT01 lies immediately west of the currently active WVZ.

The results of the GA inversion of interstation Rayleigh-wave dispersion curves for station pairs in western Iceland were used as reference models for receiver-function inversion, because they represent the broad structures of the interstation areas. The models used were path HOT01–HOT05 (for station HOT01), path HOT02–HOT05 (for station HOT02), path HOT05–HOT11 (for station HOT11) and path HOT03–HOT05 (for stations HOT03 and HOT04) (Fig. 1).

Good fits to the receiver functions were achieved for all backazimuths at station HOT01 (Fig. 8), and the structures are constrained at all depths to be within a model covariance of 0.2, except for three control nodes where 0.1 was used. There is fair agreement with the structures determined using earthquakes from the three different backazimuths. The high velocity gradients characteristic of the upper crust in Iceland are observed in the upper 6.5–7.5 km, and below this overall velocity gradients are much lower. The level at which V_s reaches ~4.1 km s^{-1} coincides with a steep rise in V_s from ~4.0 to ~4.5 km s^{-1} over an interval of ~5 km. The best estimate of the depth to the base of the lower crust is ~22 km. A short interval of relatively high velocity gradients is preferred by the data from the north and southwest backazimuths but not by the data from the east backazimuth. Some backazimuthal structural variation is expected because the east-backazimuth receiver functions sample the crust and upper mantle beneath the WVZ that lies immediately east of station HOT01. In contrast, the north and southwest backazimuth receiver functions sample intraplate regions that do not comprise currently active or extinct rift zones.

There are four surface wave models available as candidate starting models for the station HOT05 receiver function inversions. We use the models from paths HOT02–HOT05 and HOT01–HOT05 for the southwest and north backazimuthal inversions, respectively. We try both the models from paths HOT05–HOT11 and HOT03–HOT05
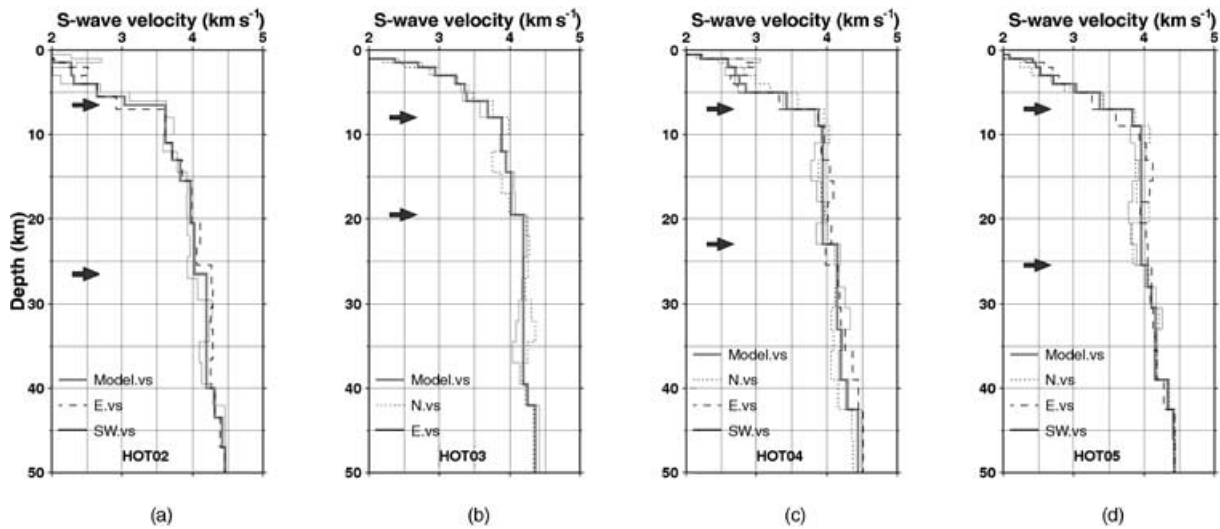
Figure 9. Summary of receiver function inversion results for stations HOT02, HOT03, HOT04 and HOT05. The smoothest model from each backazimuth is shown as thin solid, dotted and dashed lines, along with an overall average model (thick grey line). Arrows show the depths at which V_s reaches 3.7 km s^{-1} and the depth beneath which it does not fall below 4.1 km s^{-1}, which are the best estimates of the depths to the bases of the upper and the lower crusts.

for the eastern backazimuthal receiver function inversion. Three control nodes at depths of 7, 19 and 30 km were used, where we limit C_m to be 0.1. Because the surface wave dispersion measurements constrain velocity contrasts weakly, it is important to use constraints only where the reference model displays smooth structures. It can be seen from comparing the models of paths HOT05–HOT11 and HOT03–HOT05 (Fig. 6) that even the GA inversion is not able to assess the significance of the small-scale, 3-D structures, but their long-wavelength features are compatible, i.e. both models are similar at depths of ∼7, 19 and 30 km. Consequently, use of either of the two different initial models results in similar final results.

The receiver-function inversion results for stations HOT02–HOT05 are shown in Fig. 9. For all stations the results for data from different backazimuths are fairly consistent, yielding best estimates for the depths to the bases of the upper and lower crusts of

6.5–7.5 and 20–26 km, respectively. The shallowest estimate of the depth to the base of the lower crust obtained anywhere in Iceland using receiver functions is the 20 km depth observed beneath station HOT03, at the foot of the Snaefellsjokull volcano. The amplitude of the velocity discontinuity where V_s rises above 4.1 km s^{-1} is 0.2 km s^{-1} beneath station HOT03. Beneath stations HOT02, HOT04 and HOT05, it varys with backazimuth and is ∼0.2–0.3 km s^{-1}, which comprises a relatively weak constraint on the depth to the crust–mantle transition.

Only data from the east and southwest backazimuths are available for station HOT11 (Fig. 10). The depth where V_s exceeds 3.7 km s^{-1} is 7 km, although a clear change from steep to very low gradients does not occur until a depth of ∼9 km (Fig. 10c). A rise in gradient occurs again at ∼30 km. There is considerable uncertainty in the crustal thickness beneath this station and five control points from the
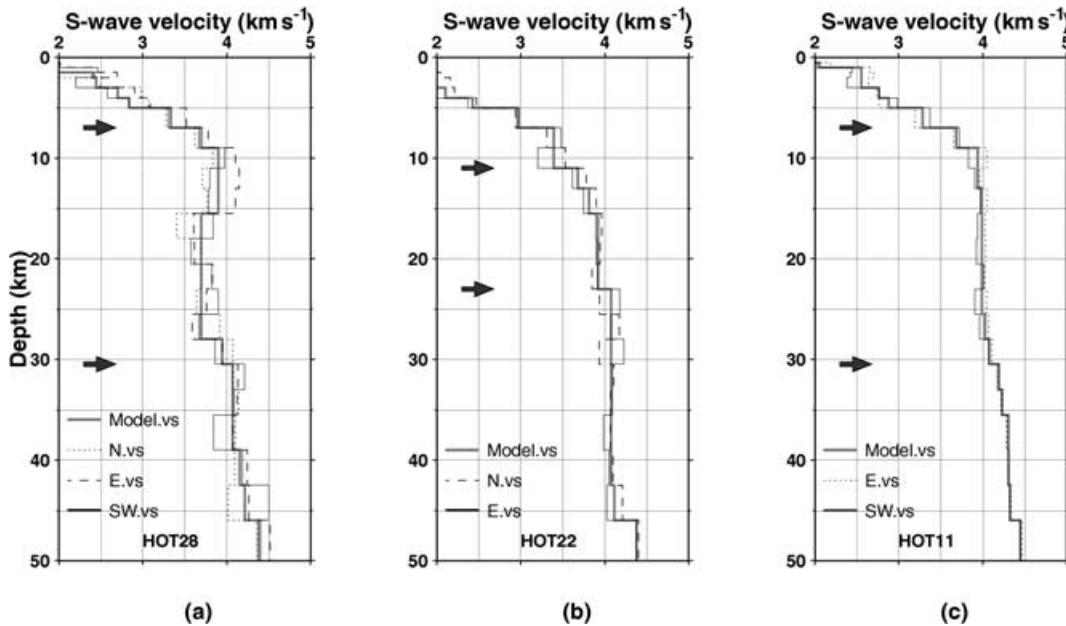

Figure 10. Same as in Fig. 9, but for stations HOT28, HOT22 and HOT11.

GA inversion for the path structure of HOT05–HOT11 were used. The structures obtained from the surface wave inversion (Fig. 6d) and the receiver-function inversion (Fig. 10c) are very similar, but an acceptable fit to the receiver functions is only achieved for the first 8 s of the waveforms. The structure obtained here is similar to that obtained for station HOT12 (Du & Foulger 2001).

Station HOT28 lies within the MVZ (Fig. 1). No interstation surface wave dispersion curve was available local to station HOT28 so the starting model used was obtained by simplifying a model for station SKR, which has a constant-velocity lower crust and a gradational transition from crustal to mantle velocities starting at ∼38 km (Du & Foulger 2001). We conducted a non-constrained receiver-function inversion (Fig. 10a). We found variability in the results using data from the three backazimuths, but all the results feature an upper crust that is ∼7 km thick beneath which a velocity inversion occurs. This is consistent with the structures determined beneath stations HOT26, HVE and SKR, which also lie in or close to the MVZ, and where lower-crustal low-velocity zones (LVZs) were also observed (Du & Foulger 2001). The depth to the base of the lower crust beneath station HOT28 is estimated to be ∼30 km, shallower than the ∼38–40 km determined beneath other stations in the MVZ (Du & Foulger 2001).

Station HOT22 lies south of the EVZ (Fig. 1). The results from receiver-function inversion are shown in Fig. 10(b). The starting model used was obtained from interstation surface wave dispersion curves for path HOT22–HOT21 and not HOT22–SKR, since the latter crosses the neovolcanic zone, which is expected to have a different structure from the Tertiary block within which station HOT22 lies (Du & Foulger 2001). An unusually large thickness of 11 km for the upper crust is obtained, with a very small velocity discontinuity of only ∼0.15 km s^{-1} marking the transition to velocities of 4.1 km s^{-1} at a depth of 24 km.

Crustal structures beneath stations in eastern Iceland

The receiver-function inversion results for stations in western Iceland are summarized in Fig. 11. In the cases of stations HOT18 and HOT29, sufficient data were available for the east backazimuthal receiver-function data set to be subdivided into two groups: east-southeast ($\alpha = 108°–125°$, $\Delta = 34°–42°$) and east-northeast

($\alpha = 70°–89°$, $\Delta = 53°–71°$) (Fig. 12). The two groups differ in average backazimuth by about 16°. Event waveforms are consistent within each group but they differ significantly between the two groups. The reference models used were the average models from the GA inversion for path HOT18–HOT15 (for station HOT15), path HOT18–HOT29 (for station HOT29), path HOT18–HOT17 (for station HOT17) and path HOT16–HOT19 (for stations HOT16 and HOT19). Three path-average models are available for station HOT18. The shallow levels (0–8 km) of the path HOT18–HOT15 model are characterized by the steepest velocity gradients. We invert the north backazimuthal receiver function of HOT18 using the path HOT18–HOT15 model as a starting model. While we consider the GA models for paths HOT18–HOT17 and HOT18–HOT29 are similar if the constraints are taken from ∼5, 15 and 35 km depths, respectively. Therefore, we use the path HOT18–HOT17 model as a starting model for other two backazimuthal inversions.

Because the structural results for stations HOT15, HOT16 and HOT29 were fairly similar, we show them together in Fig. 11(d). A clear change from the high velocity gradients that characterize the upper crust to the low velocity gradients that characterize the lower crust occurs beneath all stations at a depth of ∼7–9 km. The depth at which the velocity exceeds 4.1 km s^{-1} varies from 27 km beneath station HOT18 (Fig. 11b), where it is marked by a velocity discontinuity of ∼0.45 km s^{-1} over an interval of a few kilometres, to 33 km beneath station HOT17, where small velocity discontinuities of <0.22 km s^{-1} in total occur. At the other stations, the base of the lower crust is marked only by an increase in the velocity gradient over a thick interval starting at ∼30 km.

The structures obtained from separate inversion of the two groups of receiver functions at stations HOT18 and HOT29 exhibit significant differences (Fig. 13). These results were obtained by defining C_m using the error bounds of the GA models. Constraints were put at depths of 5, 14 and 31 km for station HOT18 and at 5, 16 and 33 km for station HOT29 where the GA models display smooth structures. Comparing Figs 13(a) and (b) with Figs 7(c) and (b), significant differences may be seen between the initial and final models. The receiver function inversions recovered shorter-wavelength features than would be possible using just surface waves. Three control nodes retain the long-wavelength features, and no additional information was needed to remove the ambiguity inherent in the receiver
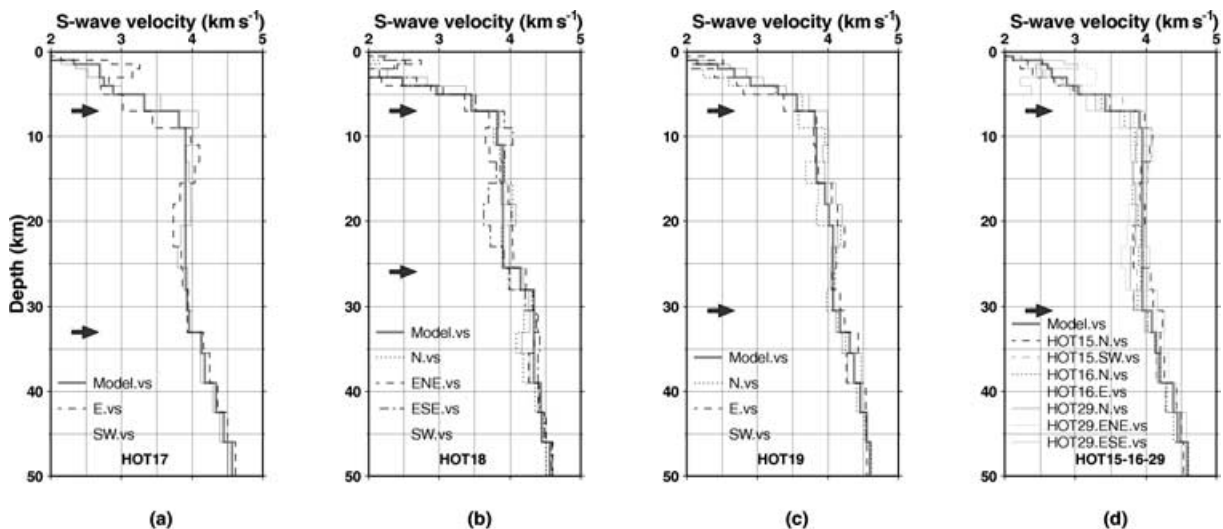

Figure 11. Same as in Fig. 9, but for stations in eastern Iceland. The rightmost panel shows the results for stations HOT15, HOT16 and HOT29 together, since the results were similar.
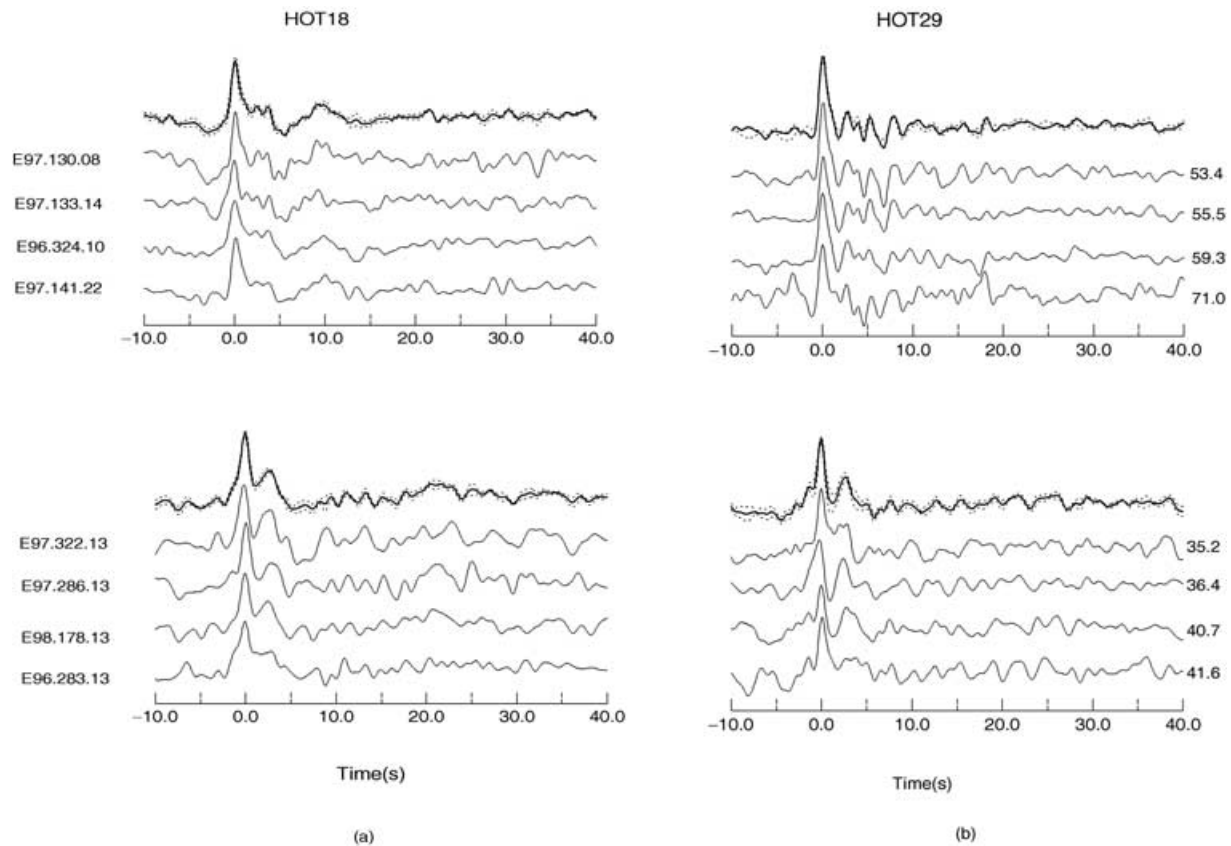
Figure 12. Same as in Fig. 2, but for the east-southeast (top panels) and the east-northeast (bottom panels) backazimuths for stations (a) HOT18 and (b) HOT29.

function inversions. For both stations, the best estimates for the depths to the bases of the upper and lower crusts are fairly consistent at 7 km for the depth to the base of the upper crust, and ~26 and ~31 km for the depths to the base of the lower crust. For both stations a tripartite structure is obtained. The main differences in

the structures determined from the two backazimuths are that the data from the east-southeast backazimuth require anomalously high velocities at the base of the upper crust, exceeding the 4.0 km s^{-1} usually attributed to the base of the lower crust, and a lower-crustal LVZ. These significant differences in the structural results from close backazimuths highlight the 3-D nature of the Icelandic crust.
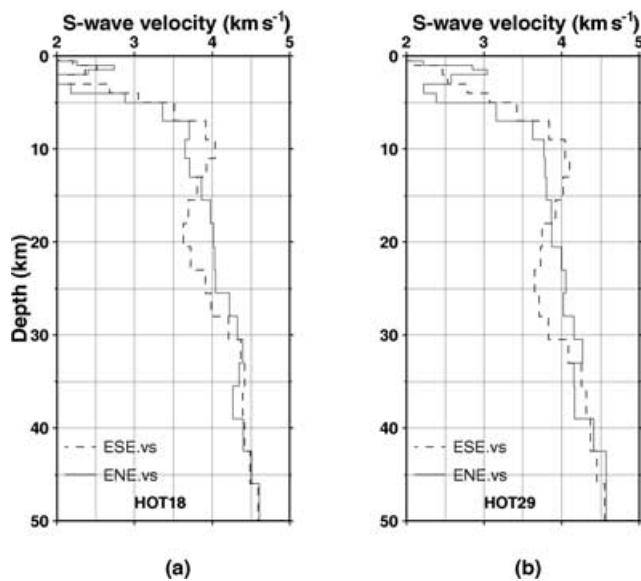
SUMMARY AND DISCUSSION

The approach we use in this paper to combining surface wave dispersion data and receiver-function data is more powerful than methods used previously (e.g. Du & Foulger 1999, 2001). Joint inversion is only appropriate if the volumes sampled by the two data sets are either the same, or similar in structure. The decision regarding relative weights to assign to the two types of data are also subjective and potentially influential. The approach used by Du & Foulger (2001), who jointly modelled surface wave dispersion curves, the waveforms of a large regional earthquake and receiver functions, yielded average structures with relatively large error bars. In this paper, we first invert surface wave dispersion curves by globally searching model space, and in this way we eliminate the problem of arbitrarily choosing a starting model that may lead to convergence to a local minimum in parameter space. By using the results of GA surface wave inversion as a starting model for receiver-function inversion, we may be confident that the inversion procedure starts with a model that is close to the global minimum. The receiver-function inversion is also subjected to a few constraints from the surface wave inversion result that exclude unreasonable competing models.
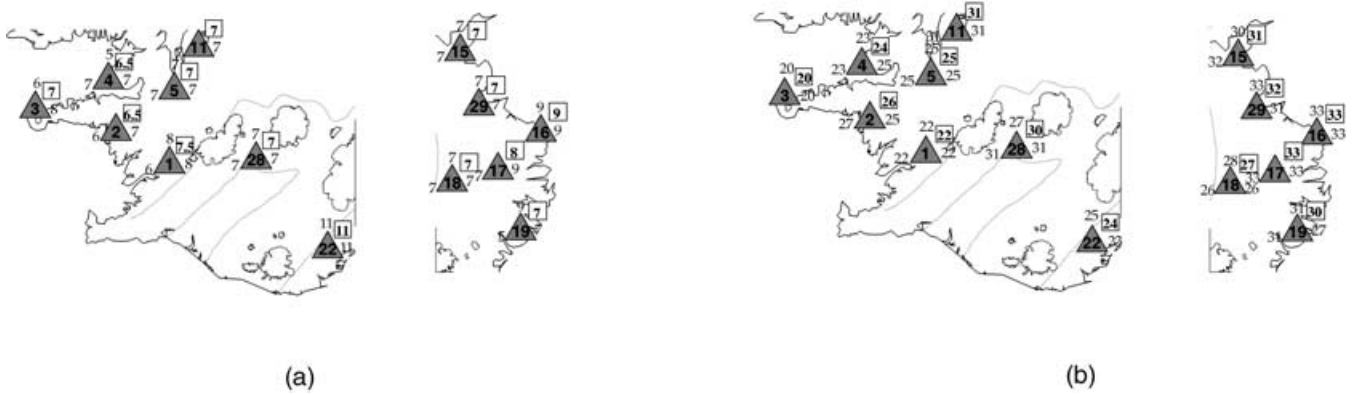

Figure 13. Summary of receiver function inversion results for stations HOT18 and HOT29 for the east-southeast (dashed lines) and the east-northeast (thin, solid lines) backazimuths.

(a)   (b)

Figure 14. Maps of eastern and western Iceland showing the best estimates for depths to the bases of (a) the upper, and (b) the lower crusts. These are taken to be the depths at which (a) V_s reaches 3.7 km s^{-1}, and (b) beneath which V_s does not fall below 4.1 km s^{-1}. Triangles indicate the stations, and the numbers within indicate the station number. Unboxed numbers, depths obtained from inverting data from individual backazimuths. The positions of the digits around the stations indicate the backazimuths of the earthquakes used. Boxed numbers, averages from all backazimuths. The neovolcanic zones and glaciers are outlined.

Inversion of the surface wave dispersion curves yields broad, smoothed structures, and subsequent receiver-function inversion adds detail. Some generalizations may be drawn from the results of surface wave inversion. Enhanced velocity gradients in the top ~10 km, beneath which velocity gradients are small or zero, characterize the structure beneath all areas studied. Some profiles additionally exhibit deeper zones of increased velocity gradient. Structures lacking zones of increased gradient at depth typically have velocities in the lower crust of ~4.0 km s^{-1}, whereas structures with high gradients at depth exhibit velocities of ~3.8–3.9 km s^{-1}. The former paths are all sampled by surface waves approaching from the southwest backazimuth, parallel to the tectonic fabric of Iceland and the trends of dykes and fissure swarms. The Icelandic crust is expected to exhibit substantial anisotropy, with the fast direction SSW–NNE and the slow direction normal to this. Thus, anisotropy in the lower crust may explain these observations. This could be studied further in future using tangential receiver functions, and high-quality data from many backazimuths, at such time as suitable data become available. Fig. 14 summarizes our estimates of the depths to the bases of the upper and lower crusts. Although the sites we study in this paper are mostly outside the currently active rift zones, we nevertheless observe considerable backazimuthal variation, suggesting that crustal structure is highly 3-D, even in Tertiary intraplate areas. These areas are rich in extinct fissure swarms and central volcano complexes, and Snaefellsnes is a volcanically active flank zone, so this finding is not surprising. For all stations except HOT22, the thickness of the upper crust is estimated to lie in the range 6.5–9 km. This is in agreement with observations from elsewhere in Iceland (e.g. Du & Foulger 1999, 2001). The depth at which V_s exceeds 3.7 km s^{-1} is generally, but not always, close to a fairly clear change in structure where high velocity gradients of up to ~0.45 s^{-1} in V_s at shallow depth give way to low velocity gradients of ≲0.02 s^{-1} beneath. This level may represent the depth at which all cracks and fractures are closed by overburden pressure. The exceptionally large thickness of upper crust observed beneath station HOT22 is in agreement with the results of Flovenz (1980), who found a remarkable thickening of the upper crust in this region from waveform modelling of explosion seismology data. This thickening may be related to the exceptionally large volcanic productivity of this region, and the progressive loading of the surface with glacial and jokulhlaup debris.

Beneath the upper crust, although there is some variation with backazimuth, and variation between stations in western Iceland, the results are fairly uniform in showing a thick sequence with a small overall velocity gradient punctuated with occasional minor velocity discontinuities. Using a definition for the base of the lower crust as the level beneath which V_s does not fall below 4.1 km s^{-1}, depths in the range ~20–26 km are obtained for all stations. Inspection of the results for individual stations, however, shows that there is great variability in the clarity of this boundary and the backazimuthal variation. For example, beneath station HOT04, depths of between ~13 and 26 km might be considered within the noise (Fig. 9c). In Fig. 14 we present estimates of the depths to the upper and lower crusts strictly according to our definition. Because there is significant backazimuthal variation in structure, and we are able to sample only a few backazimuths, meaningful errors in our depth estimates cannot be quantified, but it may be seen from the variations in structure determined for individual stations in Figs 8–11 that the uncertainty is considerable. Larger velocity discontinuities, of ~0.2–0.25 km s^{-1} are observed at depths of ~20 and ~27 km beneath stations HOT03 and HOT18 (Figs 9b and 11b). These are end-member results, and in most other cases the velocity discontinuity at the $V_s \sim 4.1$ km s^{-1} level is smaller. In the cases of many of the results, if error bounds of ~±0.1 km s^{-1} are assumed, a broad range of estimates might be made for the depth to the base of the lower crust.

The detection of a velocity inversion in the lower crust beneath station HOT28 provides evidence that the LVZ detected beneath stations HOT26, HVE and SKR by Du & Foulger (2001) extends over an area beneath the MVZ at least 10 000 km^2 in size. It does not extend as far as station HOT14, however, as shown by waveform modelling of a regional event (Du & Foulger 2001). This area coincides with the centre of the low-velocity anomaly detected beneath Iceland by teleseismic tomography (Foulger *et al.* 2000, 2001). The LVZ occupies the depth range ~15–28 km beneath station HOT28, but typically ~15–35 km beneath the other stations. It is thus 13–20 km thick. Candidate explanations are that it is caused by a locally high geothermal gradient or partial melt. Interestingly, such an LVZ is not observed beneath the currently active rift zones (e.g. Darbyshire *et al.* 2000; Du & Foulger 1999, 2001).

The extreme 3-D heterogeneity of the Icelandic crust is reflected in the significant backazimuthal variation in the results commonly seen, and exemplified by the results from the east-northeast and east-southeast backazimuths at stations HOT29 and HOT18. Station HOT29 lies within a double central volcano complex with at least three calderas (Johannesson & Saemundsson 1998), and significant

3-D heterogeneity is expected there. Station HOT18 is, however, located in upper Miocene rock away from significant central volcano complexes, and no geological explanation for the backazimuthal structural variation observed is obvious. Heterogeneity is expected in the currently active rift zones, which are assemblages of fissure and dyke swarms and central volcanoes. Outside of these zones, Tertiary intraplate areas are also complex and inhomogeneous, being densely punctuated by extinct rift zones and volcanic systems. The kinematics of accretion results in systematic variations in the dip of lavas in the upper crust relative to the lateral position of the rift zone at which they were produced (Palmason 1980), and frequent rift migrations on all scales provide additional complications. Our results highlight the fact that nowhere in Iceland may be considered simple and homogeneous.

Where our stations lie close to long explosion seismology profiles, the results may be compared. Stations HOT01 and HOT02 lie fairly close to the northwest end of the 170 km long South Iceland Seismic Tomography (SIST) profile (Fig. 1) (Bjarnason *et al.* 1993). Using a V_p/V_s ratio of 1.76 (Menke *et al.* 1996), a velocity of $V_p = 6.5$ km s^{-1} would correspond to the value of $V_s = 3.7$ km s^{-1} we use for the base of the upper crust. At the northwest end of the profile, the depth to this horizon is ∼6 km away from central volcano complexes. This agrees with our estimate of 6.5–7.5 km. A depth of ∼21–22 km was obtained for the base of the lower crust from the SIST data. We obtain an estimate of ∼22 km for this horizon beneath the station HOT01. Further towards the west, the base of the lower crust deepens. Beneath station HOT02, our best estimate is ∼26 km.

The Faroe–Iceland Ridge Experiment (FIRE) profile (Fig. 1) lies within ∼35 km of stations HOT17, HOT18 and HOT19 (Staples *et al.* 1997). Beneath this part of the profile, a depth of ∼8 km was determined to the $V_p = 6.5$ km s^{-1} horizon, which agrees well with our estimate of ∼7–8 km for the base of the upper crust at these three stations. A depth of ∼33 km was obtained for the base of the lower crust from the FIRE data. It is reasonable to compare this with our estimates of depth to the base of the upper crust since Staples *et al.* (1997) estimate basal crustal velocities of 7.1–7.35 km s^{-1}, corresponding to $V_s = 4.03$–4.18 km s^{-1}, which is close to the $V_s = 4.1$ km s^{-1} we use. We obtain an estimate of ∼33 km for this horizon beneath the nearest station, HOT17. We estimate a depth of ∼27 km beneath station HOT18, which is close to the eastern edge of the NVZ. This result agrees qualitatively with the findings of Staples *et al.* (1997) who found the base of the lower crust to shallow towards the NVZ.

As we found in earlier studies of crustal structure using receiver-function inversion, there is considerable variability in the nature and clarity of the crust–mantle transition from type 1 structures (e.g. station HOT01, Fig. 8) to type 2 structures (e.g. station HOT05, Fig. 9d). The most consistent feature of our present and previous results is the clear division into an upper sequence with high velocity gradients and a lower sequence with low velocity gradients. In western and eastern Iceland the depth to the base of the upper crust is typically ∼6.5–9 km. The depth to the base of the lower crust is more difficult to estimate because velocity profiles are characterized by low overall gradients in the lower crust and small discontinuities. For those profiles that do not show significant velocity discontinuities or relatively narrow intervals of enhanced velocity gradients at velocities corresponding to the expected crust–mantle transition, estimates made of the depth to the base of the lower crust based on velocity may have large uncertainties when the variation of the backazimuth and the inherent error in the data are taken into account. Nevertheless, the depths we estimate are fairly consistent at

∼20–26 km for stations in western Iceland and ∼27–33 km for stations in eastern Iceland. Within these ranges, the most extreme values occur beneath or close to the currently active rift zones and major volcanoes, e.g. Snaefellsjokull.

A model of a simple Icelandic crust clearly divided into upper and lower parts, and separated from the normal mantle by a clear Moho is ill-suited to describing our results. It is the exception rather than the rule for the structures we observe to fit such a model naturally and imposition of such a classification scheme obscures the true nature of our observations. In particular, the use of any consistent definition for the base of the lower crust, if applied rigorously, would yield large variations in the estimated thickness of the crust over Iceland. Acceptance of a particular framework for geological interpretation brings with it a disposition to find geologically consistent results within that framework. This may lead to bias in emphasizing particular interpretations in preference to others equally well supported by the observations, and to unfounded extrapolations. Although a great deal of seismic data constraining structure is now available, the geological nature of the crust and upper mantle beneath Iceland and the transition from one to the other, are still not well understood, and the full range of candidate model interpretations that are not ruled out by the data should be considered.

ACKNOWLEDGMENTS

REFERENCES

Ammon, G.J., 1991. The isolation of receiver effects from teleseismic *P* waveforms, *Bull. seism. Soc. Am.,* **81,** 2504–2510.

Ammon, G.J., Randall, G.E. & Zandt, G., 1990. On the nonuniqueness of receiver functions, *J. geophys. Res.,* **95,** 15 303–15 318.

Angenheister, G. *et al.*, 1980. Reykjanes Ridge seismic experiment (RRISP 77), *J. Geophys.,* **47,** 228–238.

Bjarnason, I.Th., Menke, W., Flovenz, O.G. & Caress, D., 1993. Tomographic image of the mid-Atlantic plate boundary in southwestern Iceland, *J. geophys. Res.,* **98,** 6607–6622.

Darbyshire, F.A., Bjarnason, I.Th., White, R.S. & Flovenz, O.G., 1998. Crustal structure above the Iceland mantle plume imaged by the ICEMELT refraction profile, *Geophys. J. Int.,* **135,** 1131–1149.

Darbyshire, F.A., White, R.S. & Priestley, K.F., 2000. Structure of the crust and uppermost mantle of Iceland from a combined seismic and gravity study, *Earth planet. Sci. Lett.,* **181,** 409–428.

Davis, L. (ed), 1990. Genetic algorithms and simulated annealing, in *Research Notes in Artificial Intelligence,* Pitman, London.

Du, Z.J. & Foulger, G.R., 1999. The crustal structure beneath the Northwest Fjords, Iceland, from receiver functions and surface waves, *Geophys. J. Int.,* **139,** 419–432.

Du, Z.J. & Foulger, G.R., 2001. Variation in the crustal structure across central Iceland, *Geophys. J. Int.,* **145,** 246.

Flovenz, O., 1980. Seismic structure of the Icelandic crust above layer three and the relation between body wave velocity and the alteration of the basaltic crust, *Tectonophysics,* **189,** 1–17.

Flovenz, O. & Gunnarsson, K., 1991. Seismic crustal structure in Iceland and the surrounding area, *J. Geophys.,* **47,** 211–220.

Foulger, G.R. *et al.*, 2000. The seismic anomaly beneath Iceland extends down to the mantle transition zone and no deeper, *J. Geophys.,* **142,** F1–F5.

Foulger, G.R. *et al.*, 2001. Seismic tomography shows Iceland is underlain by an upwelling confined to the upper mantle, *Geophys. J. Int.,* **146,** 504–530.

Goldberg, D.E., 1989. *Genetic Algorithms in Searching, Optimization, and Machine Learning,* Addison-Wesley, Reading, MA.

Johannesson, H. & Saemundsson, K., 1998. *Geological Map of Iceland, 1:500,000, Tectonics,* Icelandic Institute of Natural History, 1st edn, Reykjavik.

Langston, C.A., 1979. Structure under Mount Rainier, Washington, inferred from teleseismic body waves, *J. geophys. Res.,* **84,** 4749–4762.

Levshin, A.L., Ratnikova, L. & Berger, J., 1992. Peculiarities of surface-wave propagation across central Eurasia, *Bull. seism. Soc. Am.,* **82,** 2464–2493.

Levshin, A.L., Ritzwoller, M.H. & Ratnikova, L.I., 1994. The nature and cause of polarization anomalies of surface-waves crossing northern and central Eurasia, *Geophys. J. Int.,* **117,** 577–590.

Lomax, A. & Snieder, R., 1995. The contrast in upper mantle shear-wave velocity between the east European platform and tectonic Europe obtained with genetic algorithm inversion of Rayleigh-wave group dispersion, *Geophys. J. Int.,* **123,** 169–182.

Menke, W., Brandsdottir, B., Einarsson, P. & Bjarnason, I.Th., 1996. Reinterpretation of the RRISP-77 Iceland shear-wave profiles, *Geophys. J. Int.,* **126,** 166–172.

Menke, W., West, M., Brandsdottir, B. & Sparks, D., 1998. Compressional and shear velocity structure of the lithosphere in northern Iceland, *Bull. seism. Soc. Am.,* **88,** 1561–1571.

Palmason, G., 1980. A continuum model of crustal generation in Iceland; kinematic aspect, *J. Geophys.,* **47,** 7–18.

Saemundsson, K., 1979. Outline of the geology of Iceland, *Jokull,* **29,** 7–28.

Sambridge, M. & Drijkoningen, G., 1992. Genetic algorithms in seismic waveform inversion, *Geophys. J. Int.,* **109,** 323–342.

Staples, R.K., White, R.S., Brandsdottir, B., Menke, W., Maguire, P.K.H. & McBride, J.H., 1997. Faeroe–Iceland Ridge Experiment 1. Crustal structure of northeastern Iceland, *J. geophys. Res.,* **102,** 7849–7866.

Tarantola, A., 1987. *Inverse Problem Theory: Methods for Data Fitting and Model Parameter Estimation,* Elsevier, Amsterdam.